Role of carbon and hydrogen in limiting *n*-type doping of monoclinic $(Al_xGa_{1-x})_2O_3$

Sai Mu [1], Mengen Wang [1], Joel B. Varley [2], John L. Lyons [3], Darshana Wickramaratne [3], and Chris G. Van de Walle [1,*]

[1]*Materials Department, University of California, Santa Barbara, California 93106-5050, USA*
[2]*Lawrence Livermore National Laboratory, Livermore, California 94450, USA*
[3]*Center for Computational Materials Science, United States Naval Research Laboratory, Washington, DC 20375, USA*

We use hybrid density functional calculations to assess *n*-type doping in monoclinic $(Al_xGa_{1-x})_2O_3$ alloys. We focus on silicon, the most promising donor dopant, and study the structural properties, formation energies, and charge-state transition levels of its various configurations. We also explore the impact of carbon and hydrogen, which are common impurities in metal-organic chemical vapor deposition (MOCVD). In Ga_2O_3, Si_{Ga} is an effective shallow donor, but in Al_2O_3 Si_{Al} acts as a *DX* center with a $(+/-)$ transition level in the band gap. Interstitial hydrogen acts as a shallow donor in Ga_2O_3 but behaves as a compensating acceptor in *n*-type Al_2O_3. Interpolation indicates that Si is an effective donor in $(Al_xGa_{1-x})_2O_3$ up to 70% Al, but it can be compensated by hydrogen already at 1% Al. We also assess the diffusivity of hydrogen and study complex formation. Si_{cation}-H complexes have relatively low binding energies. Substitutional carbon on a cation site acts as a shallow donor in Ga_2O_3, but can be stable in a negative charge state in $(Al_xGa_{1-x})_2O_3$ when $x > 5\%$. Substitutional carbon on an oxygen site (C_O) always acts as an acceptor in *n*-type $(Al_xGa_{1-x})_2O_3$, but will incorporate only under relatively oxygen-poor conditions. C_O-H complexes can actually incorporate more easily, explaining observations of carbon-related compensation in Ga_2O_3 grown by MOCVD. We also investigate C_{cation}-H complexes, finding they have high binding energies and act as compensating acceptors when $x > 56\%$; otherwise the hydrogen just passivates the unintentional carbon donors. C-H complex formation explains why MOCVD-grown Ga_2O_3 can exhibit record-low free-carrier concentrations, in spite of the unavoidable incorporation of carbon. Our study highlights that, while Si is in principle a suitable shallow donor in $(Al_xGa_{1-x})_2O_3$ alloys up to high Al compositions, control of unintentional impurities is essential to avoid compensation.

I. INTRODUCTION

Monoclinic Ga_2O_3 (β-Ga_2O_3) is a wide-band-gap material (4.76–5.1 eV [1–4]) with a high breakdown field (6–8 MV/cm) [5]. Despite its wide band gap, Ga_2O_3 can be controllably *n*-type doped; together with the availability of high-quality yet low-cost substrates these properties render β-Ga_2O_3 highly promising for applications in high-power electronics and UV optoelectronics [6–8].

Effective control of the carrier concentration by doping with shallow donors is essential for device applications. This typically requires that the donor impurity has a low ionization energy and that compensation can be avoided. Si, Ge, and Sn have been demonstrated to be effective shallow donors in Ga_2O_3 with modest ionization energies ($\leqslant 80$ meV) [9–21]. In addition to these dopants, first-principles calculations have identified interstitial hydrogen (H_i) and carbon on a Ga site (C_{Ga}) as shallow donors [20,22]. Compensation of the shallow donors can occur due to native defects [23,24] or impurities that act as acceptors, or due to self-compensation if the dopant can occur in different configurations. One form of self-compensation involves the formation of substitutional species on either cation or anion sites. For example, carbon in Ga_2O_3 can occur either on the Ga site (C_{Ga}), acting as a donor, or on the O cite (C_O), acting as an acceptor [22]. Self-compensation can also occur by formation of so-called *DX* centers, in which an impurity expected to act as a shallow donor exhibits a large lattice relaxation and becomes negatively charged by trapping electrons, thus effectively acting as a deep acceptor. In Ga_2O_3, Si, Ge, and Sn do not form *DX* centers [16,20,25]. However, the likelihood of formation of a *DX* center increases as the band gap increases, as is well known for AlGaAs [26] and AlGaN alloys [27].

Alloying with Al raises the band gap of Ga_2O_3 [28,29]. Heterojunctions of $(Al_xGa_{1-x})_2O_3$ and Ga_2O_3 exhibit a high-density two-dimensional electron gas, which is at the core of field-effect transistors [30]. Modulation doping is required for high mobility, raising the issue of whether *n*-type doping of $(Al_xGa_{1-x})_2O_3$ can be achieved. Addressing this issue requires investigating whether dopants that are effective for Ga_2O_3 remain shallow donors in $(Al_xGa_{1-x})_2O_3$, and whether compensation will occur. In addition, recent experiments on $(Al_xGa_{1-x})_2O_3$ films grown by metal-organic chemical vapor deposition (MOCVD) indicated that control of doping might be challenging; it was found [31] that doping with Si failed to result in *n*-type doping below a threshold Si concentration. Above the threshold, an abrupt enhancement of the carrier

*vandewalle@mrl.ucsb.edu

concentration was observed. Identifying the origin of the compensation in $(Al_xGa_{1-x})_2O_3$ alloys is therefore important for further improvements in electronic devices.

Varley *et al.* [21] recently reported a first-principles study of *DX*-center formation for a large number of candidate donor impurities in $(Al_xGa_{1-x})_2O_3$. They found that Si emerged as the best candidate, since it continues to act as a shallow donor up to high Al concentrations in the alloy. In the present work we therefore focus on Si as the donor; we perform a more detailed study of its behavior as a *DX* center, and investigate other sources of compensation and potential complex formation.

Our study, based on hybrid density functional theory (DFT), addresses Si impurities in monoclinic Al_2O_3 (hereafter denoted as θ-Al_2O_3), and reveals a new configuration of the *DX* state. Compensation by native point defects has been previously addressed [23,24]. Here, we perform an in-depth study of compensation due to other impurities, particularly carbon and hydrogen. Both of these impurities are readily incorporated during MOCVD growth. Carbon on a cation site [22] and hydrogen [20] are both shallow donors in Ga_2O_3, but possess $(0/-)$ or $(+/-)$ charge-state transition levels in the band gap in Al_2O_3. By interpolating between the end compounds, Ga_2O_3 and Al_2O_3, we can estimate the position of these defect levels in $(Al_xGa_{1-x})_2O_3$ alloys, and determine the Al composition at which the onset of compensation occurs. (Note that we use the term "defect" to denote both native point defects and impurities.) Our results show that Si is an effective donor in $(Al_xGa_{1-x})_2O_3$ up to 70% Al, but it can be compensated by hydrogen already at 1% Al, or by carbon on cation sites at 5% Al.

Given that hydrogen is expected to be quite mobile, we also perform a study of its migration properties. We further assess the possibility of forming hydrogen-related defect complex with Si and C. Si_{cation}-H complex formation is not a major concern, since the complexes have low binding energies. Binding energies are much higher for C-H complexes; in fact, C-H behaves almost as a fixed entity, with properties very similar to a nitrogen impurity. C_{cation}-H complexes can act as compensating acceptors in $(Al_xGa_{1-x})_2O_3$ alloys, but only when the Al content exceeds 56%; otherwise the complexes are mainly neutral and hydrogen passivates the unintentional carbon donors. This may explain why MOCVD-grown Ga_2O_3 can exhibit record-low free-carrier concentrations [32], in spite of the probably unavoidable incorporation of carbon.

Substitutional carbon on an oxygen site (C_O), finally, always acts as an acceptor in *n*-type $(Al_xGa_{1-x})_2O_3$, irrespective of Al concentration. C_O will incorporate only under relatively cation-rich (oxygen-poor) conditions; we find that C_O-H complexes can actually incorporate more easily, explaining experimental observations of carbon-related compensation in Ga_2O_3 grown by MOCVD [33,34].

The paper is organized as follows. In Sec. II, the calculational details, the definition of defect formation energies, and the physics of *DX* centers are introduced. The main results for Si, C, and H and consequences for carrier compensation are presented in Secs. III A, III B, and III C, respectively; complexes are discussed in Sec. III D. Section IV concludes the paper.
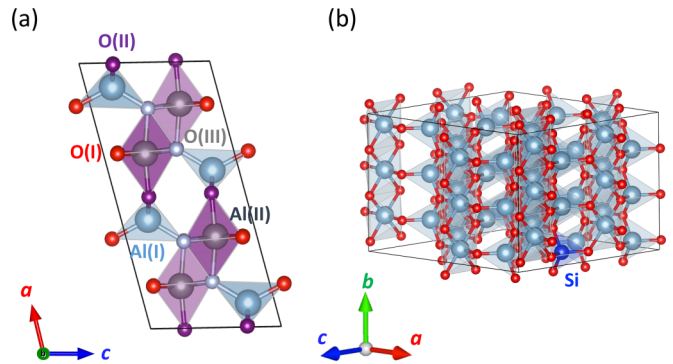

FIG. 1. (a) Conventional cell of monoclinic Al_2O_3. Two inequivalent Al sites are labeled: tetrahedrally coordinated Al(I) in aqua and octahedrally coordinated Al(II) in purple. For the O sites, threefold-coordinated O(I) are in red, threefold coordinated O(II) in purple, and fourfold- coordinated O(III) in gray. (b) Supercell constructed by creating a $1 \times 3 \times 2$ multiple of the conventional monoclinic cell of θ-Al_2O_3, with one tetrahedrally coordinated Al replaced by Si. Light blue, red and dark blue spheres denote Al, O, and Si atoms, respectively. Structural visualization was performed using VESTA [38].

II. METHODOLOGY

A. Computational details

We perform DFT calculations using the projector augmented wave method (PAW) [35] implemented in the Vienna *ab initio* simulation package (VASP) [36,37]. We focus on the monoclinic phase of Ga_2O_3 (denoted $\beta - Ga_2O_3$) and Al_2O_3 ($\theta - Al_2O_3$). The structure, illustrated in Fig. 1(a), contains two types of cation sites: the tetrahedral site (denoted as I) and the octahedral site (denoted as II). In addition, there are three types of O atoms: three-fold coordinated O(I) (on a shared corner of two edge-sharing AlO_6 octahedra and one AlO_4 tetrahedron), threefold coordinated O(II) (on the shared corner of one AlO_6 octahedron and two AlO_4 tetrahedra), and fourfold coordinated O(III).

A plane-wave energy cutoff of 400 eV was employed and Brillouin-zone integration was carried out using the Γ-centered $4 \times 4 \times 4$ k-point mesh for the primitive cell and $2 \times 2 \times 2$ for the supercell. The PAW potentials correspond to the valence-electron configurations $4s^2 4p^1$ for Ga, $3s^2 3p^1$ for Al, and $2s^2 2p^4$ for O. To correctly describe the electronic structure as well as charge localization we use a hybrid functional, specifically the functional of Heyd, Scuseria, and Ernzerhof (HSE) [39], with a mixing parameter of $\alpha = 0.32$. This produces a band gap of 4.83 eV for β-Ga_2O_3 and 7.41 eV for θ-Al_2O_3, in good agreement with the experimental band gaps of 4.80 for β-Ga_2O_3 and 7.40 eV [40] for θ-Al_2O_3. An ordered $AlGaO_3$ alloy is also investigated, with all Al atoms on octahedral sites and all Ga atoms on tetrahedral sites [28]. The use of an ordered structure serves as an approximation; the computation of structures representative of disordered alloys would be computationally prohibitive. We note that for the 50% Al content, ordered $AlGaO_3$ was found to be a line compound due to the preference for Al to occupy octahedral sites [28]. Spin polarization is included and full structural optimizations were performed. The optimized

TABLE I. Structural parameters (lattice parameters in angstroms; angle β in degrees), formation enthalpy per formula unit (ΔH_f, eV/f.u.), and band gaps (E_{gap}, eV) for monoclinic Ga_2O_3, $AlGaO_3$ and Al_2O_3. Experimental results are also listed for comparison.

	Ga_2O_3		$AlGaO_3$		Al_2O_3	
	Calc	Expt	Calc	Expt	Calc	Expt
a	12.14	12.21[a]	11.86	12.00[a]	11.66	11.85[e]
b	3.02	3.04[a]	2.94	2.98[a]	2.88	2.90[e]
c	5.78	5.81[a]	5.69	5.73[a]	5.57	5.62[e]
β	103.77	103.87[a]	104.25	104.03[a]	104.04	103.83[e]
ΔH_f	−10.22	−11.29[b]	−13.87		−16.11	
E_{gap}^{indir}	4.83		5.81		7.41	7.40[f]
E_{gap}^{dir}	4.87	4.76[c], 4.88[d]	5.89		7.74	

[a]Reference [41]; [b]Reference [42]; [c]Reference [2]; [d]Reference [3]; [e]Reference [43]; [f]Reference [40].

computed structural parameters of β-Ga_2O_3, $AlGaO_3$ and θ-Al_2O_3 are summarized in Table I; they compare favorably with experiment.

A 120-atom supercell was constructed for the point-defect calculations, as shown in Fig. 1(b). Selected tests were performed using 160-atom supercells. Tests for larger supercells are too expensive to perform with the hybrid functional, but supercell size convergence was further checked using the generalized gradient approximation of Perdew, Burke, and Ernzerhof (PBE) [44] for Si and C impurities in supercells containing up to 1280 atoms. Transition levels were found to change by less than 0.1 eV. For each point defect, we perform multiple calculations with different symmetry-breaking initial local distortions around the defect in the initial state, and optimize the atomic positions until the Hellmann-Feynman forces are lower than 5 meV/Å. All the supercell calculations are consistently performed at the lattice parameters obtained with the same plane-wave energy cutoff, as listed in Table I.

Migration barriers are calculated using the climbing-image nudged elastic band (cNEB) method [45]. To mitigate computational cost we perform one-shot HSE calculations for the migration barriers (E_b): we use PBE [44] in the cNEB calculations, followed by static HSE total energy calculations based on the initial and barrier geometries. We tested the accuracy of this approach for the migration of H_i^+ in Al_2O_3 and Ga_2O_3 along the [010] direction; full HSE calculations yield migration barriers that are within 0.1 eV of the results obtained using one-shot HSE calculations.

After determining the migration barrier of a defect, we can estimate the temperature at which the defect becomes mobile with transition state theory [46]. This temperature is denoted as an "annealing temperature," above which the defect is in thermodynamical equilibrium. In transition state theory [46], the rate Γ at which the defect hops to a neighboring site can be expressed as

$$\Gamma = \Gamma_0 \exp\left(-\frac{E_b}{k_B T}\right), \qquad (1)$$

where k_B is the Boltzmann constant and E_b the migration barrier. The prefactor Γ_0 is an effective frequency associated

with the vibration of the defect; for the H interstitial in both Ga_2O_3 and Al_2O_3, we choose $\Gamma_0 = 10^{14}$ s^{-1}, which is approximately the dominant O-H vibrational frequency Ga_2O_3 [23,47]. We estimate the annealing temperature as the temperature at which the rate $\Gamma = 1$ s^{-1} [48]. We note that the annealing temperature is not very sensitive to the choice of Γ_0.

B. Formation energy

The formation energy of a defect is used to assess the likelihood of the presence of the defect and its concentration. For Si substituting on an Al site (Si_{Al}), the formation energy is calculated as

$$E^f(Si_{Al}^q) = E_{tot}(Si_{Al}^q) - E_{tot}(Al_2O_3) - \left(\mu_{Si} + \mu_{Si}^0\right)$$
$$+ \left(\mu_{Al} + \mu_{Al}^0\right) + q(E_F + E_{VBM}) + \Delta^q, \qquad (2)$$

where $E_{tot}(Si_{Al}^q)$ is the total energy of one Si_{Al} in charge state q in the supercell, $E_{tot}(Al_2O_3)$ is the total energy of the bulk supercell, and E_F is the Fermi energy, referenced to the valence-band maximum (VBM). Δ^q is a finite-size correction term for charged defects [49,50]. We adopt the previously reported values for the dielectric constants of Ga_2O_3, $AlGaO_3$, and Al_2O_3 [21]. The chemical potentials are referenced to the elemental phases, e.g., $\mu_{Si}^0 = E_{tot}(Si)$ and $\mu_{Al}^0 = E_{tot}(Al)$.

The Al and O chemical potentials have to fulfill the stability condition for bulk Al_2O_3:

$$2\mu_{Al} + 3\mu_O = \Delta H_f(Al_2O_3), \qquad (3)$$

where $\Delta H_f(Al_2O_3)$ is the formation enthalpy of bulk θ-Al_2O_3, as shown in Table I. The calculated formation enthalpies of β-Ga_2O_3 and $AlGaO_3$ are listed in Table I as well. $\mu_{Al} = 0$ corresponds to Al-rich conditions, and $\mu_O = 0$ to O-rich (Al-poor) conditions. For purposes of presenting results for the impurities, we choose the chemical potentials to correspond to the solubility limit, i.e., the highest value of the chemical potential that is compatible with formation of other phases that can result from interactions of the impurity with the host elements. For μ_{Si}, this correspond to equilibrium with SiO_2:

$$\mu_{Si} + 2\mu_O = \Delta H_f(SiO_2), \qquad (4)$$

where $\Delta H_f(SiO_2)$ is the calculated formation enthalpy of SiO_2. For C and H, the upper limits depend on the host chemical potentials: the limits for μ_C correspond to Al_4CO_4 for Al-rich and CO_2 for Al-poor conditions; the limits for μ_H correspond to H_2 for Al-rich and H_2O for Al-poor.

To be able to comment on the behavior in $(Al_xGa_{1-x})_2O_3$ alloys, we also calculate formation energies in Ga_2O_3. The limiting phases for Si and H are the same as those in the Al_2O_3 case. The limits for μ_C in Ga_2O_3 correspond to graphite for Ga-rich and CO_2 for Ga-poor conditions. We note that this is different from Ref. [22], where diamond was assumed as the limiting phase under Ga-poor conditions.

The charge-state transition level between charge states q and q', denoted as (q/q'), is calculated based on the formation energies:

$$(q/q') = \frac{E^f(Si_{Al}^q; E_F = 0) - E^f(Si_{Al}^{q'}; E_F = 0)}{(q' - q)}. \qquad (5)$$
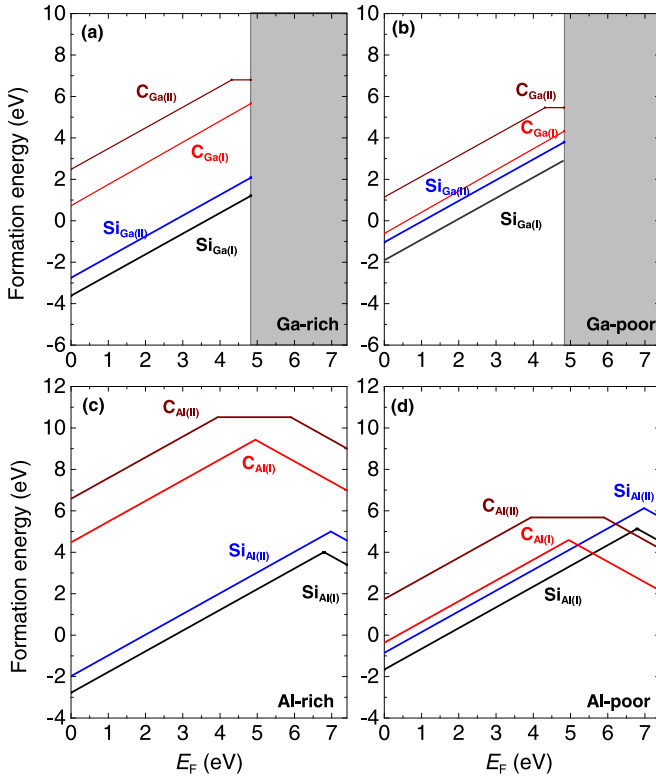
FIG. 2. Formation energy versus Fermi level for Si and C impurities in [(a) and (b)] β-Ga$_2$O$_3$ and [(c) and (d)] θ-Al$_2$O$_3$. (a) and (c) are for cation-rich, and (b)–(d) for cation-poor conditions. The grey area indicates the conduction band of β-Ga$_2$O$_3$.

C. Stability of DX centers

Following Chadi and Chang [26], we label the neutral and positively charged donors on the substitutional site d^0 and d^+, respectively. DX^- is used to denote the configuration in the negative charge state. The formation of a DX center leads to self-compensation, as described by the process

$$2d^0 \longrightarrow d^+ + DX^-. \quad (6)$$
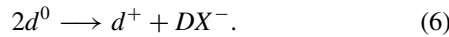
The DX center can be characterized by the effective correlation parameter U, defined by

$$U = E^f(d^+) + E^f(DX^-) - 2E^f(d^0). \quad (7)$$

Stability of the DX center is typically characterized by a negative value of U. However, using U as the descriptor of the DX center can be problematic because of the challenges involved in accurately calculating the energy of the neutral charge state when the $(+/0)$ level (and hence the Kohn-Sham state for d^0) is near or above the conduction-band minimum (CBM). Instead, we will use the $(+/-)$ charge-state transition level as a descriptor: our criterion will be that the DX center is stable if the $(+/-)$ level lies below the CBM.

III. RESULTS AND DISCUSSION

A. Silicon

The formation energies of Si on the tetrahedral (Si$_{Al(I)}$) and octahedral (Si$_{Al(II)}$) sites in θ-Al$_2$O$_3$ are shown in Figs. 2(c) and 2(d) for cation-rich and cation-poor conditions. For

TABLE II. Charge-state transition levels (eV) [Eq. (5)] and effective correlation parameter U (eV) [Eq. (7)] for various impurities in β-Ga$_2$O$_3$, ordered AlGaO$_3$, and θ-Al$_2$O$_3$. The neutral and negative charge states that are used to compute charge-state transition levels and U all correspond to localized states. Values for Si in Ga$_2$O$_3$ are missing since the localized neutral and negative charge states cannot be stabilized. We also list x^{onset} (%), the Al concentration in (Al$_x$Ga$_{1-x}$)$_2$O$_3$ corresponding to the onset of DX behavior.

β-Ga$_2$O$_3$	$(+/0)$	$(+/-)$	$(0/-)$	U	x^{onset}
C$_{\mathrm{Ga(I)}}$	5.20	4.92	4.65	−0.54	
C$_{\mathrm{Ga(II)}}$	4.32	5.05	5.77	1.46	
H$_i$	5.47	4.84	4.21	−1.25	
H$_{\mathrm{O(I)}}$	5.47	5.20	4.91	−0.55	
H$_{\mathrm{O(II)}}$	4.98	5.01	5.04	0.07	
H$_{\mathrm{O(III)}}$	5.71	5.56	5.42	−0.29	
AlGaO$_3$	$(+/0)$	$(+/-)$	$(0/-)$	U	
Si$_{\mathrm{Ga(I)}}$	6.39	6.19	6.00	−0.39	
Si$_{\mathrm{Al(II)}}$	6.065	6.46	6.85	0.79	
C$_{\mathrm{Ga(I)}}$	4.93	4.81	4.69	−0.24	
C$_{\mathrm{Al(II)}}$	4.05	4.97	5.90	1.86	
H$_i$	5.70	4.67	3.65	−2.05	
H$_{\mathrm{O(I)}}$	5.92	5.69	5.45	−0.47	
H$_{\mathrm{O(II)}}$	5.60	5.21	4.83	−0.77	
H$_{\mathrm{O(III)}}$	5.69	5.70	5.71	0.02	
θ-Al$_2$O$_3$	$(+/0)$	$(+/-)$	$(0/-)$	U	
Si$_{\mathrm{Al(I)}}$	6.77	6.79	6.81	0.04	70%
Si$_{\mathrm{Al(II)}}$	7.20	6.98	6.76	−0.44	81%
C$_{\mathrm{Al(I)}}$	4.96	4.95	4.95	−0.01	5%
C$_{\mathrm{Al(II)}}$	4.23	5.07	5.90	1.95	51%
H$_i$	5.83	4.83	3.84	−1.99	1%
H$_{\mathrm{O(I)}}$	6.51	6.36	6.41	−0.10	37%
H$_{\mathrm{O(II)}}$	5.78	5.70	5.61	−0.16	13%
H$_{\mathrm{O(III)}}$	6.11	6.12	6.13	0.03	41%

completeness and consistency, we also show the formation energies of Si in Ga$_2$O$_3$ in Figs. 2(a) and 2(b); these have been calculated previously [20] and our results are consistent with the previous results. Note that in Fig. 2 (and all subsequent formation-energy figures) we keep the horizontal-axis scale the same for β-Ga$_2$O$_3$ and θ-Al$_2$O$_3$, which facilitates comparisons of formation energies. In principle, we could also take the valence-band alignment between β-Ga$_2$O$_3$ and θ-Al$_2$O$_3$ into account to more accurately compare charge-state transition levels [51,52]; however, since the valence-band offset is relatively small [28], we do not include this alignment.

Similar to β-Ga$_2$O$_3$, Si prefers to be incorporated on the tetrahedral site in θ-Al$_2$O$_3$: $E^f(\mathrm{Si}_{\mathrm{Al(I)}}^+)$ is lower than $E^f(\mathrm{Si}_{\mathrm{Al(II)}}^+)$ by 0.80 eV. In β-Ga$_2$O$_3$ Si behaves as a shallow donor on either site, i.e., only the positive charge state is stable for all Fermi-level positions within the band gap. In θ-Al$_2$O$_3$ a $(+/-)$ charge-state transition level occurs in the band gap, at 0.62 eV below the CBM for Si$_{\mathrm{Al(I)}}$ and at 0.43 eV below the CBM for Si$_{\mathrm{Al(II)}}$ (see Table II). Table II also lists values for the other transition levels. For Si$_{\mathrm{Al(I)}}$, there is a small region of stability for the neutral charge state; we found $(+/0)$ and $(0/-)$ transition levels at 6.77 and 6.81 eV, respectively,
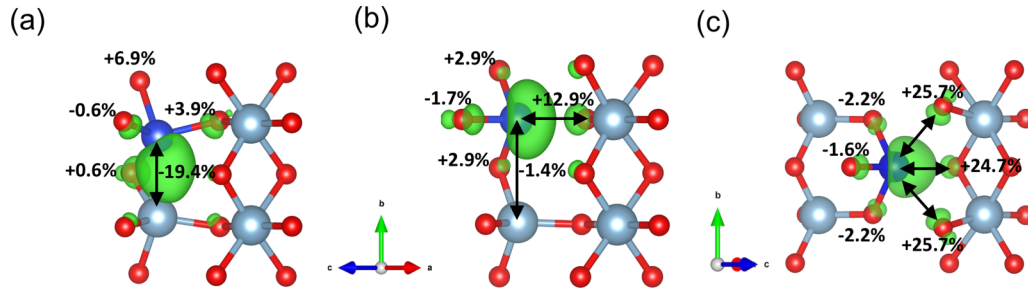
FIG. 3. Local structure and localized charge density for negatively charged DX configurations of (a) ground-state $Si^-_{Al(I)}$, (b) metastable-state $Si^-_{Al(I)}$, and (c) $Si^-_{Al(II)}$ in θ-Al_2O_3. Dark blue spheres denote Si, light blue Al, and red O. Percentage changes of bond lengths, referenced to bonds in bulk Al_2O_3, are indicated. Isosurfaces of the charge density ($0.02\,e/\text{Å}^3$) of the localized state in the DX centers are shown in green.

corresponding to $U = 0.04$ eV. For $Si_{Al(II)}$, the $(+/0)$ level lies above the $(0/-)$ level and we have a negative-U center (i.e., the neutral charge state is never thermodynamically stable), with $U = -0.44$ eV.

For Fermi levels in the upper part of the gap, Si_{Al} is in a negative charge state, associated with the formation of a DX center. For $Si_{Al(I)}$ we found that *two* locally stable DX configurations exist. The local geometry and the charge density of the localized electrons are illustrated in Fig. 3. Figure 3(a) corresponds to the ground state of $Si^-_{Al(I)}$, while Fig. 3(b) represents a metastable state that is 0.40 eV higher in energy. The metastable state [Fig. 3(b)] features the type of broken bond that is often considered characteristic of a DX center, resulting in a dangling bond on the Si atom that is filled with two electrons. The ground state of $Si^-_{Al(I)}$ [Fig. 3(a)] also displays significant bond distortions, both in the SiO_4 tetrahedron and its nearest AlO_4; however, no clear bond breaking occurs. Instead, the main effect of the distortion is to reduce the Si-Al distance from 2.88 Å (the distance in bulk θ-Al_2O_3) to 2.32 Å, creating a two-electron bond between Si and Al, as clearly seen in Fig. 3(a). Octahedrally coordinated $Si^-_{Al(II)}$ also forms a DX center, shown in Fig. 3(c). Three Si-O bonds are broken in the SiO_6 octahedron, and two electrons are localized on the Si dangling bond. Tests for the Si DX center in a 160-atom supercell yielded very similar local geometries, with bond lengths differing by less than 0.01 Å. The 160-atom supercell calculations yield a $(+/-)$ charge-state transition level that is within 0.05 eV of the result using a 120-atom supercell.

The formation of the silicon DX center indicates that Si cannot be a shallow donor in θ-Al_2O_3. To gain insight into its effectiveness in $(Al_xGa_{1-x})_2O_3$ alloys, we evaluate the position of the $(+/-)$ transition level and compare it with the CBM in $(Al_xGa_{1-x})_2O_3$ alloys. The negative charge state employed to compute the $(+/-)$ transition level has to correspond to a localized state. Such a localized state can be stabilized in Al_2O_3 and ordered $AlGaO_3$ alloy but not in Ga_2O_3. Therefore the $(+/-)$ transition levels in alloys are interpolated (or extrapolated towards Ga_2O_3) based on the values in Al_2O_3 and ordered $AlGaO_3$ alloy (see values in Table II). The values of the CBM are interpolated based on those in Ga_2O_3 and Al_2O_3, with the addition of bowing using a bowing parameter of 0.93 eV and assuming all of the band-gap bowing occurs in the CBM [28].

The resulting values of x^{onset}, the Al concentration at which the $(+/-)$ level moves below the CBM (i.e., the DX center becomes stable) are listed in Table II. We found Si incorporating

on the tetrahedral site will be an effective donor over a wide range of Al alloying, up to 70% Al (see Fig. 4). This value is somewhat lower than the $x^{onset}=86\%$ reported in Ref. [21]. The difference can be attributed to the fact that our calculated $(+/-)$ level in Al_2O_3 ($AlGaO_3$) is 0.12 eV (0.37 eV) lower than that in Ref. [21], due to the fact that we identified a lower-energy structure for the DX center. In addition, we find that Si on the octahedral site is also an effective donor in $(Al_xGa_{1-x})_2O_3$, up to 81% Al (see Fig. 4).

Our treatment of defect behavior in the alloy by performing linear interpolation (Fig. 4) is obviously an approximation. In the case of $(Al_xGa_{1-x})_2O_3$ alloys, it is likely to be quite reliable, due to the similarity in the properties of Al and Ga cations; indeed, we have found that the geometries of defect configurations are very similar in β-Ga_2O_3 and θ-Al_2O_3. Some degree of validation is also obtained from the results for transition levels explicitly calculated for $AlGaO_3$ alloys. As shown in Fig. 4, the results for the alloy generally fall
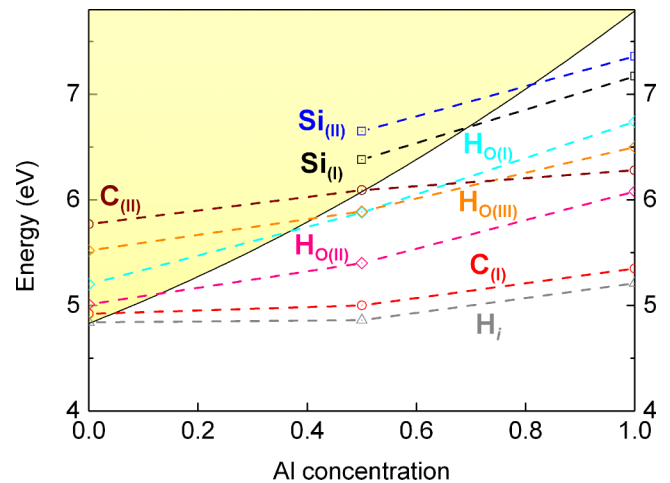

FIG. 4. The $(+/-)$ levels of $Si_{(I)}$, $Si_{(II)}$, $C_{(I)}$, H_i, $H_{O(I)}$, $H_{O(II)}$, $H_{O(III)}$, and the $(0/-)$ level of $C_{(II)}$ obtained from calculations in Al_2O_3, Ga_2O_3 and ordered $AlGaO_3$ alloys. The notation $Si_{(I)}$ and $Si_{(II)}$ denotes substitutional Si on the tetrahedral (I) and octahedral (II) cation sites, respectively, and similarly for $C_{(I)}$ and $C_{(II)}$. The charge-state transition levels for Si_I and Si_{II} in Ga_2O_3 are missing since the localized neutral and negative charge states cannot be stabilized. The dashed lines connecting the calculated values are just a guide to the eye. The CBM/VBM band offsets as a function of the Al concentration for alloys were obtained from Ref. [28].
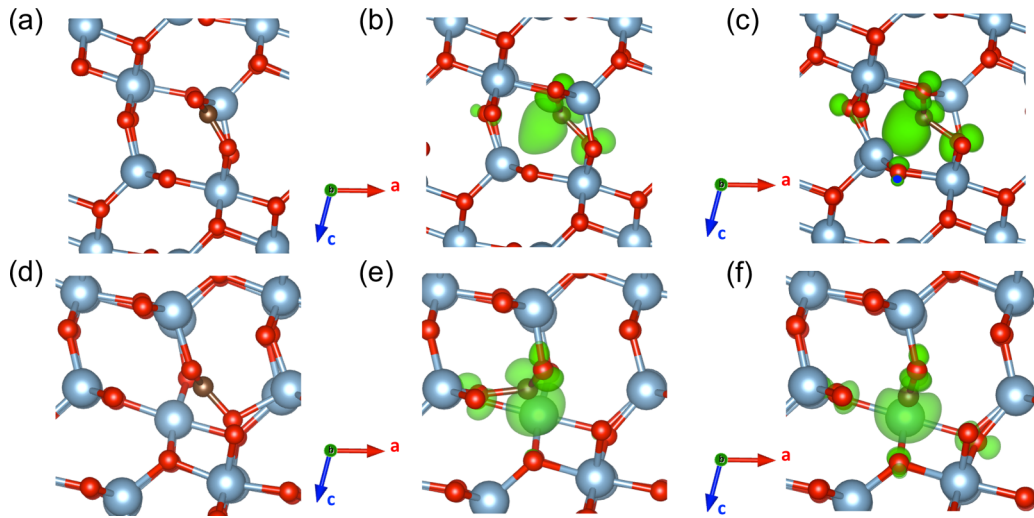
FIG. 5. Local structure and localized charge density for (a) metastable threefold-coordinated configuration of $C_{Al(I)}^+$, (b) $C_{Al(I)}^0$, (c) $C_{Al(I)}^-$, (d) $C_{Al(II)}^+$, (e) $C_{Al(II)}^0$, and (f) $C_{Al(II)}^-$ in θ-Al_2O_3. Brown spheres denote C, light blue Al, and red O. Isosurfaces of the charge density (0.01 $e/Å^3$) of the localized electrons in $C_{Al(I)}^0$, $C_{Al(I)}^-$, $C_{Al(II)}^0$, and $C_{Al(II)}^-$ are shown in green.

on the line that linearly interpolates between β-Ga_2O_3 and θ-Al_2O_3; the small deviations that occur for $C_{(I)}$ and H_i impurities amount to less than 0.15 eV, which is gratifying agreement. We also note that this interpolation procedure has been demonstrated to be effective for obtaining transition levels in AlGaN alloys [27,53]. Indeed, experiment [54] indicated that the O_N transition level in AlGaN alloys varies *linearly* with alloy concentration, supporting the validity of linear interpolation.

B. Carbon

1. Incorporation

Carbon is a commonly observed background impurity in semiconductors, particularly in MOCVD-grown films. In Ga_2O_3, carbon on the tetrahedral site is a shallow donor [22,55]. Here we investigate whether the increase in band gap in $(Al_xGa_{1-x})_2O_3$ will cause the carbon $(+/-)$ level to drop below the CBM, turning carbon into a compensating acceptor. We also study whether carbon on the oxygen site could cause compensation.

Lyons *et al.* [22] investigated carbon impurities on the anion, cation, and interstitial sites in Ga_2O_3 and showed that under most conditions, the carbon impurity prefers the substitutional tetrahedral cation site. For a consistent comparison, we reproduced the formation energies of carbon impurities on the cation sites in Ga_2O_3 [see Figs. 2(a) and 2(b)] and our results agree with Lyons *et al.* [22] under the same condition. Similar to the case of Ga_2O_3, C prefers to occupy the tetrahedral site $(C_{Al(I)}^+)$ in monoclinic Al_2O_3, with a formation energy 2.10 eV lower than that of $C_{Al(II)}^+$ at the VBM (see Fig. 2). At the CBM, the formation energy of $C_{Al(I)}^-$ is 2.03 eV lower than that of $C_{Al(II)}^-$. The behavior of C_{Al}^- as a compensating center is broadly consistent with previous results for carbon in $\alpha - Al_2O_3$, the corundum phase [56]. Figure 2 also shows that under Al-rich conditions the formation energy of $C_{Al(I)}^-$ is high, significantly decreasing when we move to Al-poor conditions.

However, carbon incorporation in MOCVD-grown samples is likely not governed by thermodynamic equilibrium, but rather determined by unintentional incorporation due to incomplete dissociation of metal-organic precursors. In the following, we therefore examine both $C_{Al(I)}$ and $C_{Al(II)}$.

2. Carbon on the tetrahedral site

The small atomic size of carbon leads to bond breaking and a variety of possible local geometries, as depicted in Fig. 5. Focusing first on $C_{Al(I)}$, already in the positive charge state we find two competing configurations of $C_{Al(I)}^+$. In the most stable state (not depicted), C forms four C-O bonds, and the oxygen cage shrinks, yielding four C-O bonds with bond lengths ranging from 1.40 to 1.44 Å. In the metastable configuration [see Fig. 5(a)], which is only 87 meV higher than the ground state, the C-O(III) bond is broken, and the remaining three C-O bonds have similar lengths (1.28, 1.30, 1.30 Å) and almost lie in the same plane, with nearly $120°$ angles between the bonds. Carbon effectively forms an sp^2-bonded configuration with its three O neighbors. This threefold coordination was also found for $C_{Ga(I)}$ in Ga_2O_3 [22], with very similar C-O bond lengths (1.27–1.30 Å). The threefold-coordinated configuration is the lowest-energy configuration in Ga_2O_3 and $AlGaO_3$.

For the neutral charge state of $C_{Al(I)}$, we found that we can stabilize as many as five distinct atomic configurations, starting from initial structures in which different C-O bonds are broken in a CO_4 tetrahedron. The most stable configuration corresponds to breaking of the C-O(III) bond, forming a nonplanar CO_3 cluster, as shown in Fig. 5(b). The C-O bond lengths are 1.35, 1.39, and 1.39 Å, while the distance between C and O(III) is 2.82 Å. This configuration is similar to the threefold coordination for the positive charge state, but the carbon has moved beyond the plane of its oxygen neighbors. As seen in Fig. 5(b), the C has moved towards a next-nearest Al(I) neighbor in the same (010) plane, reducing the C-Al distance from 3.5 Å (for C on the nominal Al site) to 2.6 Å. In the process, the charge of the localized state becomes

confined between C and that next-nearest-neighbor Al atom. The fact that this state is localized clearly indicates that $C_{Al(I)}$ is not a shallow donor in θ-Al_2O_3. Indeed, the corresponding Kohn-Sham state lies 4.42 eV below the CBM.

Another configuration in which the same C-O(III) bond is broken can be stabilized with a distance of 2.38 Å between C and O(III); this configuration is only 0.05 eV higher in energy. Other configurations involve breaking a C-O(I) bond (0.80 eV higher than the ground state) or breaking a C-O(II) bond (0.91 eV higher than the ground state). The geometry in which all four C-O bonds in the CO_4 tetrahedron are maintained is also a local minimum, 0.89 eV higher in energy than the ground-state C-O(III) bond-breaking configuration.

In the negative charge state, the most stable state is similar to the ground state of $C_{Al(I)}^0$, with a broken C-O(III) bond [see Fig. 5(c)]. Other configurations can be stabilized, but with energies that are at least 1.3 eV higher than the ground state. Figure 5(c) depicts the charge density of the localized state. Comparison with Fig. 5(b) indicates that with the addition of an extra electron a C-Al bond has formed with the next-nearest-neighbor Al(I). The C-Al distance is reduced to 2.0 Å after relaxation. This is another example of a *DX* configuration in which a cation-cation bond forms, but we note the distinction with the *DX* configuration of $Si_{Al(I)}^-$ shown in Fig. 3(a): $Si_{Al(I)}^-$ bonds with a *nearest-neighbor* tetrahedral host cation, while $C_{Al(I)}^-$ bonds with a *next-nearest-neighbor* tetrahedral host cation. A similar bonding configuration for the negative charge state of carbon on the tetrahedral site is also observed in Ga_2O_3 and $AlGaO_3$.

3. Carbon on the octahedral site

Turning now to $C_{Al(II)}$, a variety of competing local geometries with different broken bonds are also present in the positive, neutral and negative charge states due to the small atomic size of carbon. In the positive charge state, the ground state corresponds to bond breaking of two C-O(III) bonds and one C-O(I) bond in the nominal octahedron, leaving the remaining three C-O bonds (1.28, 1.28, and 1.30 Å) to form a threefold coordinated configuration that is similar to the metastable configuration of $C_{Al(I)}^+$ [see Fig. 5(d)]. We also observe a competing metastable state of $C_{Al(II)}^+$ with a different 3-fold coordinated configuration that exhibits bond breaking of all three C-O(III) within the octahedron. This metastable state is 0.20 eV higher than the ground state. This 3-fold coordinated configuration with three broken C-O(III) bonds becomes the ground state in the neutral charge state [see Fig. 5(e)]. The remaining three C-O bonds form a nonplanar CO_3 cluster, with C-O bond lengths of 1.37, 1.37, and 1.41 Å. The charge of the localized state, dominated by a *p*-orbital character, is confined between C and the center of the octahedron. Another (metastable) threefold-coordinated configuration with bond breaking of two C-O(III) and one C-O(II) is 0.28 eV higher.

In the negative charge state of $C_{Al(II)}$, the most stable configuration is twofold-coordinated, with two equivalent C-O(I) bonds (1.40 and 1.40 Å) [see Fig. 5(f)]. The localized states exhibit roughly equal *p*- and *s*-orbital character and the associated charges are confined near C, with an appreciable weight at the center of the octahedron. We also find another

competing twofold coordinated metastable configuration, with one C-O(I) bond (1.26 Å) and one C-O(II) bond (1.91 Å) remaining, and with an energy 0.18 eV higher.

4. Carbon on cation sites as a compensating center

When discussing substitutional C in $(Al_xGa_{1-x})_2O_3$ alloys, C could be replacing either a Ga or an Al atom; in this section (as in Fig. 4) we use the generic notation $C_{(I)}$ to denote either $C_{Ga(I)}$ or $C_{Al(I)}$, and $C_{(II)}$ to denote either $C_{Ga(II)}$ or $C_{Al(II)}$. $C_{(I)}$ is a negative-U center across Ga_2O_3, Al_2O_3 and the ordered $(Al_xGa_{1-x})_2O_3$ alloy (see Table II). We can evaluate its $(+/-)$ transition level in the relevant range of $(Al_xGa_{1-x})_2O_3$ alloy compositions by interpolating between Ga_2O_3 and the $AlGaO_3$ alloy, with consideration of the band bowing [28] (see Fig. 4). For $C_{(I)}$, we find that the impurity starts acting as an acceptor in $(Al_xGa_{1-x})_2O_3$ alloys already at 5% Al. $C_{(II)}$ is *not* a negative-U center, but it can still act as compensating acceptor in *n*-type Al_2O_3 (see Fig. 2). To estimate the onset of $C_{(II)}$ as a compensator in $(Al_xGa_{1-x})_2O_3$ alloys, we interpolate the $(0/-)$ transition levels between Al_2O_3 and the $AlGaO_3$ alloy (see Fig. 4), finding that $C_{(II)}$ starts acting as an acceptor at 51% Al.

Our results indicate that unintentional C incorporation is a potential explanation for the lack of doping efficiency observed at low concentrations of Si in MOCVD-grown $(Al_xGa_{1-x})_2O_3$ alloys. Since unintentionally incorporated $C_{(I)}$ acts as a compensating acceptor in $(Al_xGa_{1-x})_2O_3$ with $x \geqslant 5\%$, the Si concentration needs to exceed the concentration of $C_{(I)}$ in order for Si to actually provide *n*-type doping.

5. Carbon on oxygen sites, C_O

In Ga_2O_3, it was found that C_O acts as a compensating acceptor when the Fermi level is high in the gap [22]. Reference [22] reported results for a single O site and only for O-rich conditions; in Figs. 6(a) and 6(b), we report a full set of results for C_O in Ga_2O_3. Under conditions relevant for *n*-type doping, the formation energy of C_O is lowest when the Fermi level is at the CBM under Ga-rich conditions; however, even under these extreme conditions, this formation energy is still 2.69 eV.

The formation energy of C_O can be significantly lower in Al_2O_3, as shown in Figs. 6(c) and 6(d). For Fermi levels low in the gap (which may be difficult to attain in Al_2O_3), C_O prefers the 4+ charge state. At higher Fermi-level positions, the neutral, 1−, and 2− charge states become more favorable. For Fermi levels close to the CBM, $C_{O(I)}^{2-}$ is the energetically most favorable state.

We can therefore conclude that for *n*-type doping conditions in both Ga_2O_3 and Al_2O_3, C_O acts as a compensating acceptor. The high formation energy indicates it will not be a concern in Ga_2O_3, but it could more easily incorporate in $(Al_xGa_{1-x})_2O_3$ alloys. However, as evident from Fig. 6, this sensitively depends on chemical potentials, with cation-rich (oxygen-poor) conditions posing more of a problem. We will return to this issue in Sec. III D 4.

C. Hydrogen

Hydrogen is another impurity that is commonly unintentionally incorporated, particularly in MOCVD-grown
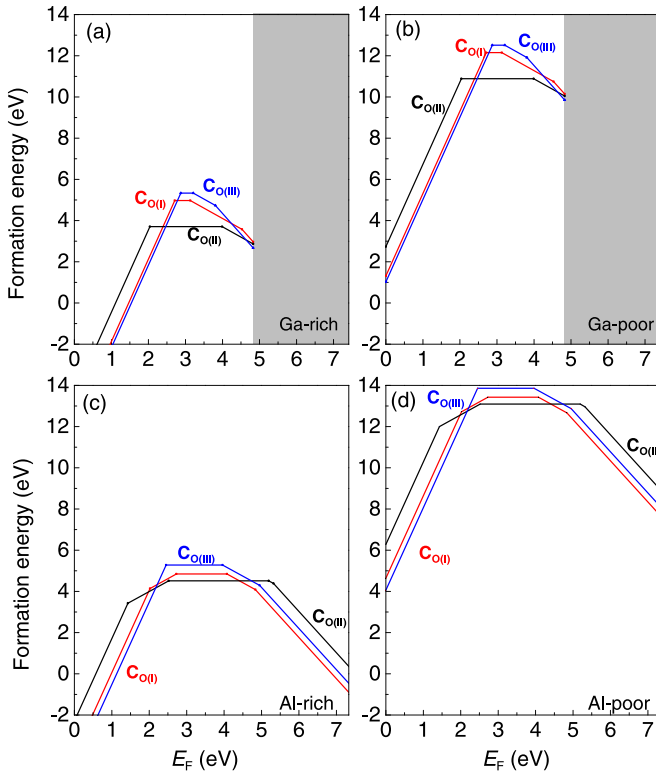
FIG. 6. Formation energy versus Fermi level for C_O in [(a) and (b)] β-Ga$_2$O$_3$ and [(c) and (d)] θ-Al$_2$O$_3$. (a) and (c) are for cation-rich and (b)–(d) for cation-poor conditions. Carbon incorporation on three possible O sites is considered: O(I), O(II), and O(III). The grey area indicates the conduction band of β-Ga$_2$O$_3$.

FIG. 7. Formation energy versus Fermi level for substitutional and interstitial hydrogen in [(a) and (b)] β-Ga$_2$O$_3$ and [(c) and (d)] θ-Al$_2$O$_3$. (a) and (c) are for cation-rich and (b)–(d) for cation-poor conditions. The grey area indicates the conduction band of β-Ga$_2$O$_3$.

samples. We investigate H substituting on the O site [$H_{O(I)}$, $H_{O(II)}$, and $H_{O(III)}$] and H on the interstitial site (H_i) in θ-Al$_2$O$_3$; their formation energies are shown in Figs. 7(c) and 7(d). For comparison, we also show our calculated formation energies in β-Ga$_2$O$_3$ [see Figs. 7(a) and 7(b)], which compare well with previous reports [20]. In β-Ga$_2$O$_3$, all these configurations were found to be shallow donors [20], but in θ-Al$_2$O$_3$, they are stabilized in the negative charge state and thus act as acceptors when the Fermi level is high in the gap.

1. Substitutional hydrogen, H_O

In Al$_2$O$_3$, substitutional H_O^+ favors incorporation on the O(I) site. Incorporation of a proton on the O(II) [O(III)] site is 0.29 [0.80 eV] higher in energy (see Fig. 7). The same site preference is also observed in the ordered AlGaO$_3$ alloy: total energies of $H_{O(II)}^+$ and $H_{O(III)}^+$ are 0.08 and 0.33 eV higher than that of $H_{O(I)}^+$, respectively. In Ga$_2$O$_3$, $H_{O(I)}^+$ is also most favorable, and $H_{O(II)}^+$ and $H_{O(III)}^+$ are slightly higher in energy [20].

Under Al-rich conditions, H_O has a low formation energy (< 2 eV) in Al$_2$O$_3$, meaning it is easy to incorporate. $H_{O(I)}$ and $H_{O(II)}$ behave as negative-U centers with $U = -0.10$ eV and -0.16 eV, and a $(+/-)$ charge-state transition level at 1.05 and 1.71 eV below the CBM (see Table II and Fig. 7). $H_{O(III)}$ is *almost* a negative-U center, with $U = +0.03$, and $(+/0)$ and $(0/-)$ charge-state transition levels at 6.11 and 6.13 eV, indicating a tiny (0.02 eV) range of stability of
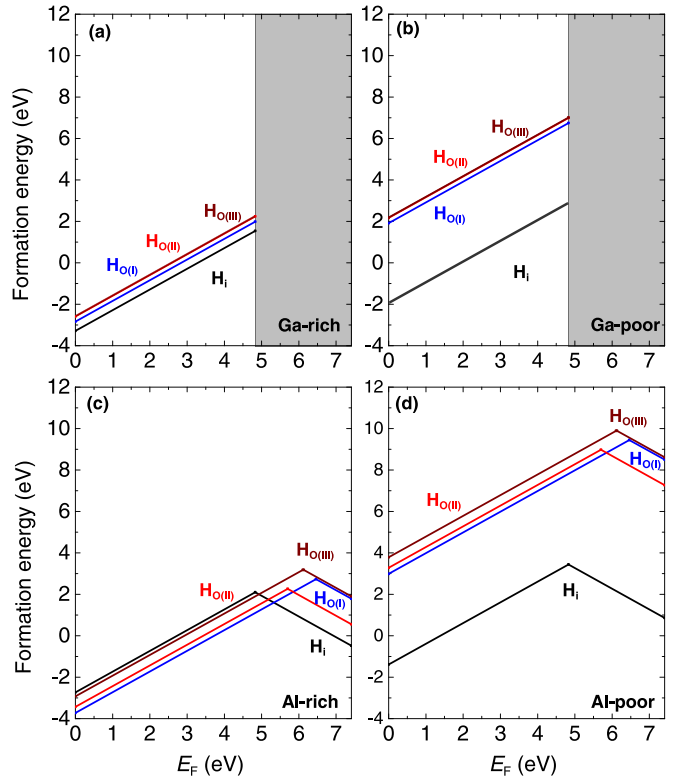
the neutral charge state. The formation of negative-U centers is due to the pronounced energy lowering in their negative charge state, induced by major local structural distortions. The local structures are illustrated in Figs. 8(a)–8(c); two electrons are localized around H and nearby Al sites. In the case of $H_{O(I)}^-$ [Fig. 8(a)], the H atom is still relatively close to the O(I) site, but the configurations of $H_{O(II)}^-$ [Fig. 8(b)] and $H_{O(III)}^-$ [Fig. 8(c)] are more like complexes of an oxygen vacancy plus a nearby interstitial H.

$H_{O(I)}$, $H_{O(II)}$, and $H_{O(III)}$ will act as acceptors in n-type (Al$_x$Ga$_{1-x}$)$_2$O$_3$ alloys due to the emergence of the $(+/-)$ transition level in the band gap starting as a critical Al composition x^{onset}. Interpolating $(+/-)$ charge-state transition levels between Ga$_2$O$_3$ and the ordered AlGaO$_3$ alloy, the onset Al concentrations for $H_{O(I)}$, $H_{O(II)}$, $H_{O(III)}$ acting as compensating centers are 37%, 13%, and 41%, respectively (see Fig. 4 and Table II).

2. Interstitial hydrogen, H_i

Turning now to interstitial H in Al$_2$O$_3$, we find that the lowest-energy configuration in the neutral and positive charge state has H bonded to the three-fold coordinated O(I). In the negative charge state, H_i prefers to sit near two Al(I) atoms; the local geometry is illustrated in Fig. 8(d). The local configurations of the $-$, 0, and $+$ state of H_i are similar to those in Ga$_2$O$_3$ [20]. In the neutral charge state, the Kohn-Sham state of H_i lies about $\sim$3 eV below the CBM. In the negative charge
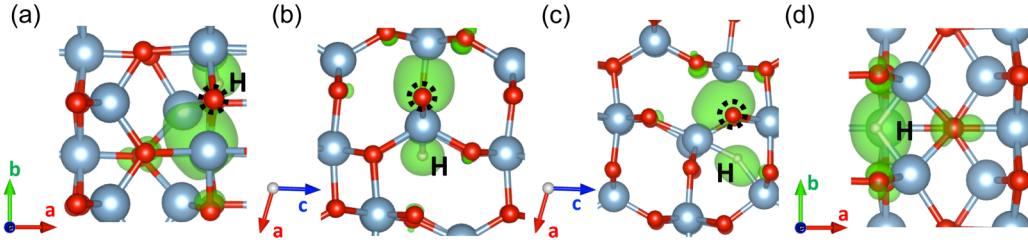
FIG. 8. Local structure of (a) $H^-_{O(I)}$ (b) $H^-_{O(II)}$, (c) $H^-_{O(III)}$, and (d) H^-_i in θ-Al_2O_3. Light blue, red and gray spheres denote Al, O, and H atoms. The position of the O atom that was removed in H^-_O was labeled using a black dashed circle. Isosurfaces of the charge density (0.01 $e/Å^3$) of the localized electrons are shown in green.

state, the Kohn-Sham state is about 1.3 eV above the VBM, as a result of the formation of two H-Al bonds.

As seen in Fig. 7 and Table II, the $(+/-)$ level of H_i in Al_2O_3 lies at 4.83 eV above the VBM. H_i is a negative-U center, with a large magnitude of $U = -1.99$ eV. Knowledge about the position of the $(+/-)$ levels in β-Ga_2O_3 and θ-Al_2O_3 allows us to estimate the band lineup between these materials, according to Ref. [57]; this leads to an alignment where the VBM of β-Ga_2O_3 lies 0.01 eV below the VBM of θ-Al_2O_3. We can compare this result with values obtained by alignment with the vacuum level derived from surface calculations; depending on the surface orientation, this procedure produces values ranging from $+0.40$ to -0.08 eV [58]. The overall agreement with the hydrogen alignment is gratifying.

Figure 7 shows that the formation energies of H_i in Al_2O_3 are quite low, suggesting that H_i will readily incorporate, and in n-type material it will act as a compensating acceptor. Following our interpolation procedure based on the case of Ga_2O_3 and ordered $AlGaO_3$ alloy, the $(+/-)$ transition level of H_i will already appear in the band gap of $(Al_xGa_{1-x})_2O_3$ alloys at an Al concentration of 1% (see Fig. 4).

3. Migration of interstitial hydrogen

Since hydrogen is expected to be quite mobile, in order to assess whether hydrogen can play a role in compensation it is important to also assess migration barriers. We investigated the migration barrier (E_b) of H_i using the PBE functional and a one-shot HSE method, as described in Sec. II A. The results are listed in Table III. The annealing temperatures at which H becomes mobile for $+$ and $-$ charge states and for various crystallographic directions, calculated using Eq. (1), are also included in Table III. As expected, the migration of

TABLE III. Calculated migration barriers (E_b, eV) of H^+ and H^- in Ga_2O_3 and Al_2O_3 along three crystallographic directions. The calculated annealing temperature (T_{anneal}, K) is listed, assuming a hopping rate of 1 s^{-1}.

	H^+			H^-		
Ga_2O_3	[010]	[100]	[001]	[010]	[100]	[001]
E_b	0.28	2.95	1.73	2.49	1.83	1.57
T_{anneal}	101	1062	623	896	659	565
Al_2O_3						
E_b	0.23	2.29	1.78	1.33	2.67	1.83
T_{anneal}	83	824	641	479	961	659

H_i in the monoclinic structure is anisotropic. In Ga_2O_3, we find the migration barrier of H^+_i along the [010] direction to be 0.28 eV, in good agreement with the 0.34 eV value reported in Ref. [20]. The migration path is illustrated in Fig. 9(a). Migration along other directions has higher barriers. Along [100] [Fig. 9(b)] the barrier is as high as 2.95 eV, and along [001] Fig. 9(c), the barrier is 1.73 eV. The annealing temperature for H^+_i migration along [010], [100], and [001] directions are 101, 1062, and 623 K, respectively.

Our calculated results for migration paths and barriers for H^+_i in Al_2O_3 are quite similar to the results in Ga_2O_3; migration is also strongly anisotropic (see Table III). The low migration barrier suggests that H^+_i can move along the [010] direction (which is the most commonly used growth orientation) even at temperatures well below room temperature.

For H^-_i, the migration barriers are generally higher. Particularly striking is that migration in Ga_2O_3 now has the highest barrier along [010] (see Table III). We attribute this to the fact that in the barrier geometry for H^-_i, the distance between H and the nearest Ga atoms is quite large (2.1 Å). Since it is Coulombic attraction between H^-_i and the cations that stabilizes the structure, the lack of strong bonding at the saddle point raises the energy. In contrast, in Al_2O_3 the corresponding distance is only 1.8 Å, providing for a stronger interaction with the Al atoms and lowering the barrier height. While the migration barriers for H^-_i are higher than for H^+_i, the annealing temperatures in Table III indicate that H^-_i may be mobile at temperatures at which growth or processing of Ga_2O_3 and $(Al_xGa_{1-x})_2O_3$ alloys is typically performed.

Figuring out precise migration barriers for H_i in $(Al_xGa_{1-x})_2O_3$ alloys may not be as simple as interpolating the values in Ga_2O_3 and Al_2O_3. The barriers to be overcome will be determined by the local environment. If, at a particular Al composition, a "percolation path" exists that allows hydrogen to follow favorable atomic arrangements, the lower of the two migration barriers will likely apply. In the absence of such a path, the higher of the two barriers will need to be overcome.

We note that the mobility of H^-_i will be reduced by binding to positively charged impurities, in particular donor dopants. Formation of a Si–H complex will increase the stability of H^-_i in the lattice and add to the overall activation energy for hydrogen motion. Therefore interstitial H^-_i, in addition to substitutional H^-_O, may play a role in compensation of shallow donors in $(Al_xGa_{1-x})_2O_3$.
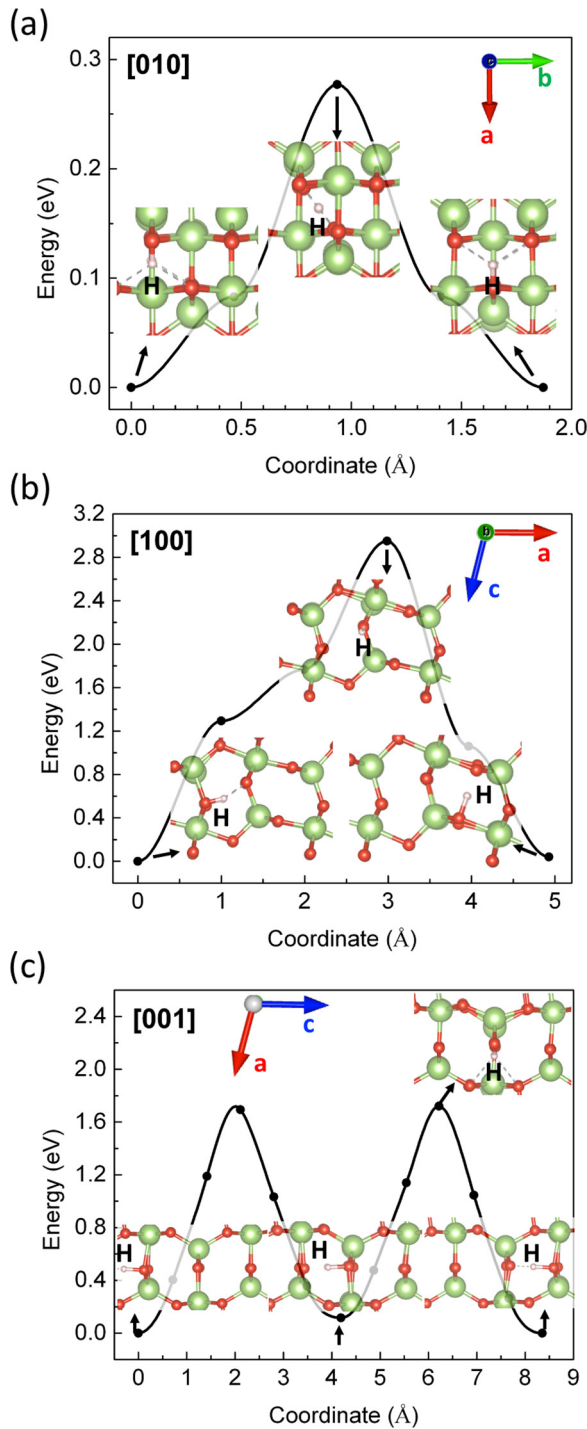
FIG. 9. Potential energy for H_i^+ migration along the (a) [010], (b) [100], and (c) [100] directions in β-Ga$_2$O$_3$. Various configurations along the migration path are shown as insets. Green and red spheres denote Ga and O atoms, respectively. Note the very different scales for the potential energy surfaces between (a) and (b) or (c).

D. Complexes

Since hydrogen can easily incorporate and has relatively low migration barriers, we need to assess the possibility of complex formation between hydrogen and other impurities, either with the intentionally incorporated Si donor, or with unintentional impurities such as C.
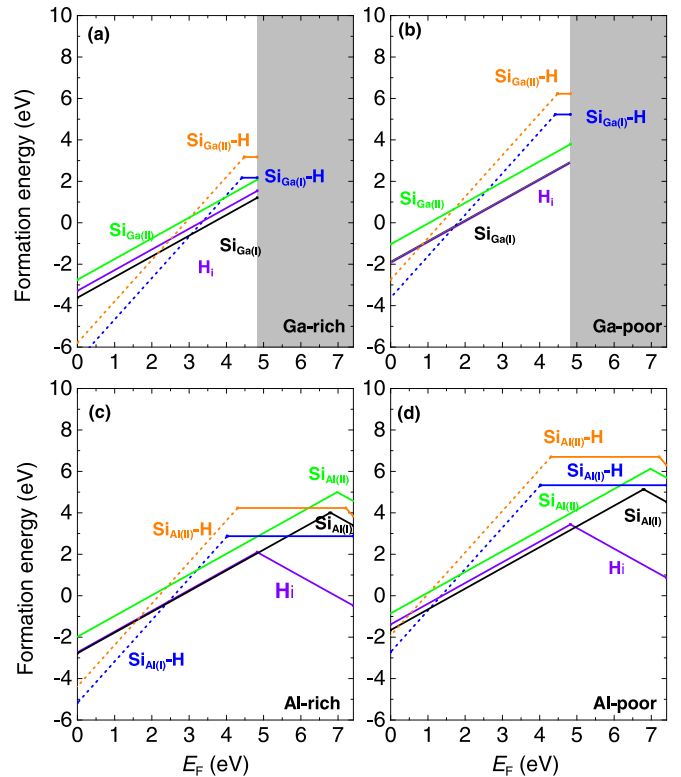

FIG. 10. Formation energy versus Fermi level for isolated Si impurities, H interstitials, and Si-H defect complexes in [(a) and (b)] β-Ga$_2$O$_3$ and [(c) and (d)] θ-Al$_2$O$_3$. (a) and (c) are for cation-rich and (b)–(d) for cation-poor conditions. Dashed lines denote thermodynamic instability of the defect complex, as explained in the text. The grey area indicates the conduction band of β-Ga$_2$O$_3$.

1. Si$_{cation}$-H *complexes*

We first discuss complexes with Si on the cation site; as discussed in Sec. III A, we found that Si$_{cation}$ is an effective donor in (Al$_x$Ga$_{1-x}$)$_2$O$_3$ alloys up to 70% Al incorporation for Si$_{(I)}$ and 81% Al incorporation for Si$_{(II)}$. The formation energy of Si–H complexes in Ga$_2$O$_3$ is shown in Fig. 10(a) for Ga-rich and Fig. 10(b) for Ga-poor conditions. We find that similar to the Si$_{Ga}$ impurity, the Si$_{Ga}$-H complex also has lower energy when Si occupies the tetrahedral cation (I) site.

The formation energy of Si–H complexes under Ga-poor conditions is simply a rigid shift to higher energies of the formation energy under Ga-rich conditions [Figs. 10(a) and 10(b)]; our discussion about the properties of complexes applies to both. We find that when the Fermi level is high in the gap, Si$_{Ga(I)}$-H complexes are stable in the neutral charge state, indicating that the Si donor has been passivated. We also find that Si$_{Ga(I)}$-H has a $(2 + /0)$ charge-state transition level at 0.41 eV below the CBM. The formation of a Si-H complex might seem unexpected, given that the constituents, Si$_{Ga}$ and H$_i$, both prefer to occur in the positive charge state throughout the band gap of Ga$_2$O$_3$, as evident from Fig. 10(a). Our calculated formation energy of point defect Si$_{Ga}$ and H$_i$ in Ga$_2$O$_3$ agree well with the previous study [20]. However, as seen in Table II, the $(+/-)$ level of H$_i$ in Ga$_2$O$_3$ lies at 4.84 eV above the VBM, i.e., just 0.01 eV above the CBM. It is therefore to be expected that for Fermi levels near the CBM,
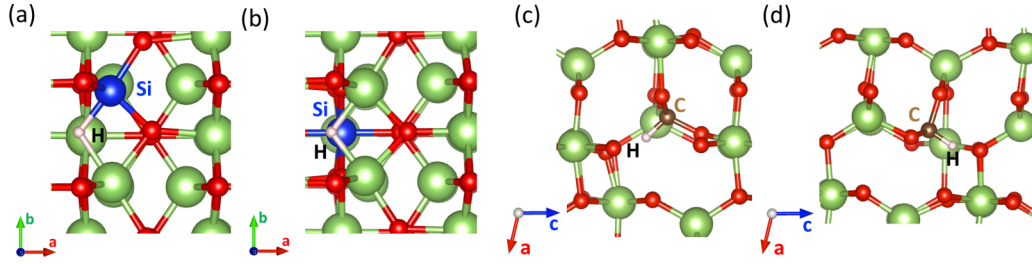
FIG. 11. Local structure of (a) $(\text{Si}_{\text{Ga(I)}} - \text{H})^0$ (b) $(\text{Si}_{\text{Ga(II)}} - \text{H})^0$, (c) $(\text{C}_{\text{Ga(I)}} - \text{H})^0$, and (d) $(\text{C}_{\text{Ga(II)}} - \text{H})^0$ in Ga$_2$O$_3$. Green, red, gray, blue, and brown spheres denote Al, O, H, Si, and C atoms, respectively.

H_i^- could be stable enough to lead to formation of a complex with Si_{Ga}^+, particularly when Coulomb attraction is taken into account.

This is confirmed by evaluation of the binding energy of the complex, defined as

$$E_{\text{bind}}[(\text{Si}_{\text{Ga(I)}} - \text{H})^0] = E^f(\text{Si}_{\text{Ga(I)}}^+) + E^f(\text{H}_i^-)$$
$$- E^f[(\text{Si}_{\text{Ga(I)}} - \text{H})^0], \qquad (8)$$

where a positive value of the binding energy signifies a stable, bound complex. This yields a binding energy of 0.59 eV. This value (which is smaller than the formation energy of each of the constituents) indicates the complex will not be stable during growth at high temperatures, since entropy favors the isolated entities (see Ref. [59]). In addition, formation after growth is not very likely since H_i will predominantly occur in the positive charge state, which is repelled by Si_{Ga}^+.

One may then wonder about the stability of $(\text{Si}_{\text{Ga(I)}} - \text{H})^{2+}$. Indeed, a binding-energy calculation in this case yields a negative value for E_{bind} (-0.24 eV), i.e., the sum of the formation energy of the constituents, $\text{Si}_{\text{Ga(I)}}^+$ and H_i^+, is smaller than the formation energy of the $(\text{Si}_{\text{Ga(I)}} - \text{H})^{2+}$ complex. We show the 2+ charge state of this complex with dashed lines in Fig. 10, to indicate that this is a locally stable configuration that is, however, thermodynamically unstable.

The notion that $(\text{Si}_{\text{Ga(I)}} - \text{H})^0$ results from bonding between $\text{Si}_{\text{Ga(I)}}^+$ and H_i^- is consistent with the local geometry of the complex: we found in Sec. III C 2 that H_i^- prefers to bind to two cation atoms on tetrahedral sites, and the configuration of $(\text{Si}_{\text{Ga(I)}} - \text{H})^0$ is such that the hydrogen atom is located close to a Ga(I) and to the Si(I) atom as seen from Fig. 11(a). This is very similar to the geometry shown in Fig. 8(d). For $(\text{Si}_{\text{Ga(I)}} - \text{H})^0$, the bond length of Si(I)-H and Ga(I)-H are 1.53 and 1.77 Å, respectively.

If the $(\text{Si}_{\text{Ga(I)}} - \text{H})^0$ complex does form during cool down, one may wonder about its stability at room temperature. The activation energy for dissociation can be estimated by adding the migration barrier for the mobile hydrogen species to the binding energy of the complex. All of the H_i^- migration barriers are large enough (Table III) to make this activation energy sufficiently high and keep the complex stable at room temperature. Using the lowest migration barrier for H_i^- in Ga$_2$O$_3$ in Table III, we would estimate an activation energy of $0.59 + 1.57 = 2.16$ eV, which would correspond to an annealing temperature of 778 K. However, since the $(2 + /0)$ transition level is so close to the CBM, an alternative dissociation mechanism could occur in which electron excitation to the CBM converts the complex to a 2+ charge state, after

which the dissociation will proceed more easily both because of the lower migration barrier of H_i^+ (Table III) and because of the Coulomb repulsion between H_i^+ and Si_{Ga}^+.

Venzie *et al.* [60] recently reported that exposure of Si-doped Ga$_2$O$_3$ to a hydrogen plasma led to passivation of the Si donor, as evidenced by a reduction in conductivity and an increase in mobility. The mobility increase indicates that the concentration of ionized-impurity centers is reduced, consistent with the formation of a complex (as opposed to mere compensation, where the compensating centers are spatially separated from the ionized donors). Venzie *et al.* [60] also proposed a geometry for the complex, which suggests that H binds to an O(I) neighbor of the Si donor; our calculations show that this configuration is 3.23 eV higher in energy than the stable geometry where H is bonded to two cations [see Fig. 11(a)]. The configuration with cation-H bonds leads to vibrational frequencies significantly lower than the 3477.6 cm^{-1} attributed to the Si-H complexes [60], suggesting that these observed modes may be due to other types of complexes that form upon hydrogenation.

The formation energy of the $\text{Si}_{\text{Ga(II)}}$-H complex is higher, but otherwise its characteristics are very similar to those of the $\text{Si}_{\text{Ga(I)}}$-H complex. The $(2 + /0)$ level of $\text{Si}_{\text{Ga(II)}}$-H in Ga$_2O_3$ occurs at 0.35 eV below the CBM (compared to 0.41 eV for $\text{Si}_{\text{Ga(I)}}$-H), and the binding energy is 0.47 eV. The local geometry of $(\text{Si}_{\text{Ga(II)}} - \text{H})^0$ is similar to that of $(\text{Si}_{\text{Ga(I)}} - \text{H})^0$, with a hydrogen binding to two nearby tetrahedral cation sites [see Fig. 11(b)]. The H-Ga bond lengths are both 1.67 Å. This reinforces the argument that a $(\text{Si}_{\text{Ga}} - \text{H})^0$ complex in Ga$_2$O$_3$ is related to the H_i^- point defect.

Similar complexes form in Al$_2$O$_3$, as seen in Fig. 10(c). The $(2 + /0)$ level of the $(\text{Si}_{\text{Al(I)}}$-H) complex occurs at $E_F = 4.02$ eV (3.39 eV below the CBM), and the binding energy of the complex is $E_{\text{bind}}[(\text{Si}_{\text{Al(I)}} - \text{H})^0] = 1.27$ eV. For $\text{Si}_{\text{Al(II)}}$-H, we find the $(2 + /0)$ transition level at 4.31 eV above the VBM (3.10 eV below the CBM), with a binding energy $E_{\text{bind}}[(\text{Si}_{\text{Al(I)}} - \text{H})^0] = 0.71$ eV.

Based on our calculated numbers, we can assess whether complex formation with hydrogen has an impact on conductivity in Si-doped (Al$_x$Ga$_{1-x}$)$_2$O$_3$ alloys. We have found the neutral complex to be stable in both Ga$_2$O$_3$ and Al$_2$O$_3$ for Fermi levels close to the CBM, and hence we expect the complex to also be stable in the alloys, with a binding energy that increases with increasing Al content. Indeed, the experiments of Venzie *et al.* [60] indicated that intentional hydrogenation can produce the complex in Ga$_2$O$_3$. However, as discussed above, the relatively modest binding energy indicates the complex will not be formed at the growth temperature. Complex
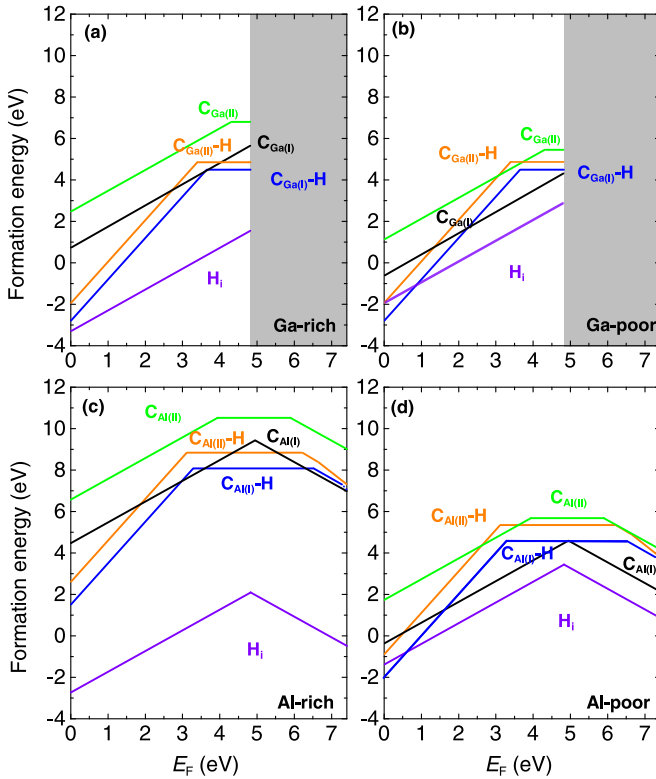
FIG. 12. Formation energy versus Fermi level for isolated C_{cation} impurities, H interstitials, and C_{cation}-H defect complexes in [(a) and (b)] β-Ga$_2$O$_3$ and [(c) and (d)] θ-Al$_2$O$_3$. (a) and (c) are for cation-rich and (b)–(d) for cation-poor conditions. The grey area indicates the conduction band of β-Ga$_2$O$_3$.

formation would therefore need to occur during cool down. Since this requires bringing H$_i$ close to a Si impurity in the positive charge state, the increasing stability of H$_i^-$ as the Al concentration increases makes complex formation more likely. If complex formation would indeed occur, annealing the sample would serve to dissociate the complex and activate the Si donor, as is well known for hydrogen-related complexes in other semiconductors [61].

2. Si$_O$ and Si$_O$-H complexes

For completeness, we also investigated Si$_O$ and Si$_O$-H complexes in both Ga$_2$O$_3$ and Al$_2$O$_3$. Formation energies are shown in Ref. [62]. Si$_O$ itself is stable in positive charge states when the Fermi level is low, but for Fermi levels close to the CBM Si$_{O(I)}$ and Si$_{O(III)}$ behave as compensating acceptors, while Si$_{O(II)}$ is neutral. However, the formation energies are so large in n-type material (even under the most favorable O-poor conditions) that they are unlikely to form or play a role in carrier compensation. Si$_O$-H complexes also act as acceptors when E_F is high in the gap, but again their formation energies are so large that they are unlikely to form.

3. C$_{cation}$-H complexes

Figures 12(a) and 12(b) show the formation energies of C-H complexes in Ga$_2$O$_3$. Similar to the Si$_{Ga(I)}$-H in Ga$_2$O$_3$, a $(2 + /0)$ charge-state transition level of C$_{Ga(I)}$-H occurs

in the band gap, at 1.18 eV below the CBM, despite the fact that the individual impurities C$_{Ga(I)}$ and H$_i$ are single donors and occur in the positive charge state throughout the band gap. Following a similar definition as in Eq. (8), we can define a binding energy relative to C$_{Ga(I)}^+$ and H$_i^-$, finding $E_{bind}[(C_{Ga(I)} - H)^0] = 2.62$ eV. This much greater value of the binding energy and lower position of the $(2 + /0)$ transition level for the C$_{Ga(I)}$-H complex as compared to the Si$_{Ga(I)}$-H complex indicates that a different type of bonding occurs. As pointed out in Sec. III D 1, $(Si_{Ga(I)} - H)^0$ can be viewed as a combination of Si$^+$ and H$^-$, with the H atom bonding to two tetrahedral cation sites [Fig. 11(a)]. In $(C_{Ga(I)} - H)^0$, on the other hand, the H atom binds to C within the tetrahedral oxygen cage, forming a strong C-H bond with a bond length of 1.06 Å [see Fig. 11(c)]. The strength of this bond, which is related to the small atomic size of C, makes the C-H combination behave as a unit, similar to a nitrogen atom, and lowers the overall formation energy. For the C$_{Ga(I)}$-H complex, the 2+ charge state is actually thermodynamically stable, i.e., it is 0.24 eV lower in energy than the sum of the formation energies of C$_{Ga(I)}^+$ and H$_i^+$. In the donor configuration of the C$_{Ga(I)}$-H complex, H is bonded to a neighboring oxygen atom within the tetrahedral oxygen cage instead of to C. This is also true for other donor (i.e., positively charged) configurations of the C$_{cation}$-H complex in both Ga$_2$O$_3$ and Al$_2$O$_3$.

Similar behavior is observed for C$_{Ga(II)}$-H: a $(2 + /0)$ transition level occurs at 2.25 eV below the CBM, and the binding energy of the neutral complex is 4.00 eV. In this case, the 2+ charge state is also thermodynamically stable, i.e., it is 1.13 eV lower in energy than the sum of the formation energies of C$_{Ga(II)}^+$ and H$_i^+$ [see Figs. 12(a) and 12(b)]. Again, a C-H bond with a bond length of 1.06 Å forms within the octahedral oxygen cage for $(C_{Ga(II)} - H)^0$ [see Fig. 11(d)]. This C-H bond formation thus indicates a unique structural feature of the C-H complex regardless of which cation site C substitutes on.

Figure 12(a) shows that C$_{Ga}$-H complexes are lower in energy than isolated C$_{Ga}$ impurities under n-type doping conditions, and this is true over most of the range of Ga chemical potentials. In addition, because of their high binding energy, such complexes may well be present during growth. Measurements of carbon concentrations in MOCVD-grown samples, in which both carbon and hydrogen are likely to be unintentionally incorporated, may thus reflect the presence of such complexes rather than isolated C$_{Ga}$ donors. Since the complexes are neutral, they would not impact the conductivity of the sample. This implicit passivation of carbon impurities, which would otherwise act as shallow donors, may well explain why MOCVD-grown Ga$_2$O$_3$ samples can exhibit free-carrier concentrations as low as 10^{14} cm^{-3} [32].

We now turn to C$_{Al}$-H complexes in Al$_2$O$_3$. Figures 12(c) and 12(d) show the formation energy of the complexes in Al$_2$O$_3$ in Al-rich conditions. The type of bonding described for Ga$_2$O$_3$ is also present in Al$_2$O$_3$, but now we see that for E_F high in the gap also a negative charge state can be stabilized, which indicates that the complex could potentially act as an acceptor and cause compensation. However, we note that the $(0/-)$ transition level of the complex occurs at a higher

position in the band gap than the $(+/-)$ transition of the isolated C_{Al}. The $(0/-)$ level of $C_{Al(I)}$-H occurs at 0.90 eV below the CBM, and a $(-/2-)$ level is also present, at 0.13 eV below the CBM. Similarly, $(0/-)$ and $(-/2-)$ levels of $C_{Al(II)}$-H are also observed close to the CBM, at 1.20 and 0.33 eV below the CBM. We note that the formation energy for $C_{Al(II)}$-H in monoclinic Al_2O_3 is similar to that in *corundum* Al_2O_3, except that the $1-$ charge state of $C_{Al(II)}$-H is absent in corundum [63]. The $C_{Al(II)}$-H bonding in monoclinic Al_2O_3 is also very similar to that in the corundum phase [63], implying that the C-H bonding within an octahedral O cage [as in Fig. 11(d)] is a host-independent structural feature.

We verified that the C_{Al}-H complexes are thermodynamically stable (i.e., have positive binding energies) in both the neutral and negative charge states. The only exception is $(C_{Al(I)} - H)^{2-}$, which has a negative binding energy. Formation of this complex is highly unlikely, anyway, since it would require the Fermi level to be within 0.13 eV of the CBM.

The stability of the C_{cation}-H complexes in the neutral and negative charge states in both Ga_2O_3 and Al_2O_3 implies they will also be stable in $(Al_xGa_{1-x})_2O_3$ alloys. The question is whether the behavior as a compensating acceptor that we find in Al_2O_3 can occur in $(Al_xGa_{1-x})_2O_3$ alloys. To assess this, we calculated the position of the $(0/-)$ transition level in Ga_2O_3 and combined this information with the results for the $(0/-)$ level in Al_2O_3. This allows us to conclude that the C_{cation}-H complexes can only occur in a negative charge state (i.e., act as acceptors) when the Al concentration exceeds 56% for $C_{(I)}$-H or 64% for $C_{(II)}$-H.

4. C_O-H *complexes*

We discussed carbon on the oxygen site, C_O, in Sec. III B 5; now we turn to its complexes with hydrogen. As shown in Fig. 13(a), C_O-H has very low formation energy in Ga_2O_3, particularly when the Fermi level is high in the gap and under Ga-rich conditions. Regardless of the O site [O(I), O(II), O(III)] on which carbon is substituting, $(+/0)$ and $(0/-)$ charge-state transition levels are present in the band gap. We verified that higher negative charge states (such as $2-$) are not stable for Fermi levels in the band gap. In all these complexes, hydrogen is always bonded to the C atom, with a bond length between 1.07 and 1.09 Å. Again, we note that the C-H unit behaves very similarly to a N impurity: C_O-H and substitutional N_O have similar $(+/0)$ and $(0/-)$ transition levels in the gap, and both behave as acceptors in *n*-type material [64].

The behavior of C_O-H in Al_2O_3 is very similar: it also only exhibits $(+/0)$ and $(0/-)$ levels in the gap, and the complex has low formation energies under Al-rich conditions and when the Fermi level is high in the gap. The binding energies of the $(C_O - H)^-$ complexes are all large in both Ga_2O_3 and Al_2O_3: all binding energies exceed 3 eV, with the exception of the $(C_{O(III)} - H)^-$ complex, where the binding energy is 1.76 eV.

We propose that the C_O-H complexes may have a distinct impact on MOCVD-grown Ga_2O_3. Seryogin *et al.* [33] grew Ga_2O_3 using a trimethylgallium (TMGa) precursor, which is known to potentially lead to increased C incorporation. They found that films grown with a lower O_2/TMGa ratio were significantly more resistive and also contained significantly more carbon. These results indicate that carbon is behaving
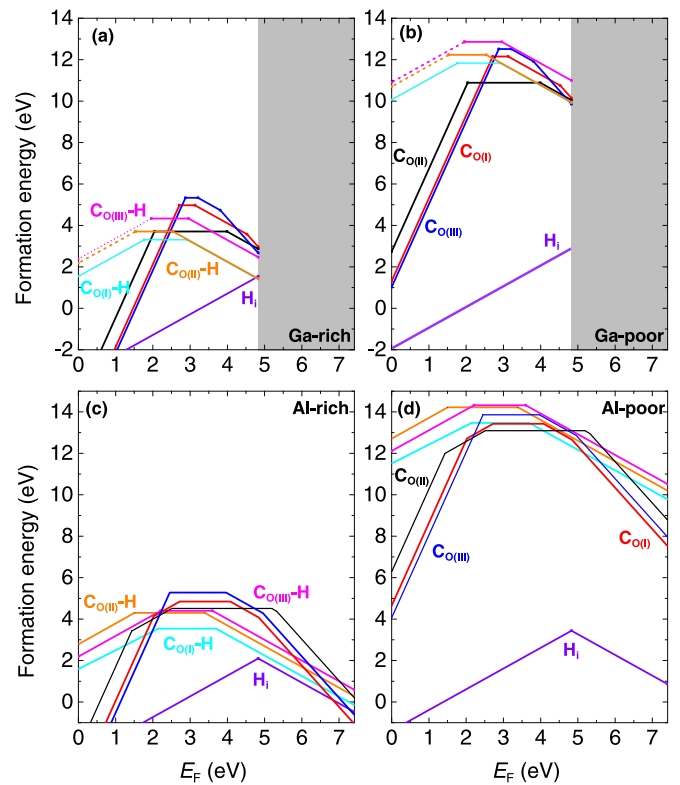

FIG. 13. Formation energy versus Fermi level for C_O impurities, H interstitials, and C_O-H defect complexes in [(a) and (b)] β-Ga_2O_3 and [(c) and (d)] θ-Al_2O_3. (a) and (c) are for cation-rich and (b)–(d) for cation-poor conditions. Dashed lines denote thermodynamic instability of the defect complex, as explained in the text. The grey area indicates the conduction band of β-Ga_2O_3.

as a compensating acceptor. The authors of Ref. [33] pointed to a computational study [65] that had found C_{Ga} to be a *DX* center in Ga_2O_3, with a $(+/-)$ level 0.81 eV below the CBM. That result is very different from ours, probably due to the particulars of the band-gap correction used in Ref. [65]. In any case, if C_{Ga} is the culprit, moving from O-rich to O-poor conditions should reduce the C_{Ga} incorporation, which is not consistent with the observed increase in C concentration. We think it is much more likely that C_O is involved, which indeed acts as a compensating acceptor with a concentration that should increase under O-poor conditions, as seen in Fig. 6. However, that figure also shows that the formation energy of C_O in the negative charge state is still relatively high, even under the most favorable (extreme O-poor and C-rich) conditions. Figure 13 indicates that this energy can be lowered by complexing with hydrogen, which should of course also be abundantly available during MOCVD growth.

The involvement of C_O-H complexes is also consistent with the experiments of Alema *et al.* [34], who found that adding H_2O vapor to the oxygen source decreased the carrier concentration, both in unintentionally doped (UID) and lightly Si-doped samples. Hydrogen could either passivate donors or form compensating acceptors. Donor passivation may occur by forming complexes with the Si donor (though in Sec. III D 1 we noted this was not very likely) or with unintentional C_{Ga} donors; for compensating acceptors, C_O-H

complexes are most likely, and indeed, Ref. [34] reported an increase in compensating acceptors rather than a decrease in donor concentration upon adding H_2O.

IV. CONCLUSIONS

We have reported a comprehensive investigation of silicon donors in $(Al_xGa_{1-x})_2O_3$ and the various ways in which they may be compensated. For Si in θ-Al_2O_3, we performed a detailed study of *DX* center formation. Two stable *DX* $Si^-_{Al(I)}$ configurations were identified, with the configuration involving bonding to two cations and no broken bonds being most energetically favorable. Interpolating the $(+/-)$ charge-state transition levels between β-Ga_2O_3 and θ-Al_2O_3, we find that Si is an effective donor over a wide range of Al concentrations in $(Al_xGa_{1-x})_2O_3$ alloys, up to 70% Al.

We also investigated the behavior of carbon and hydrogen impurities, which are commonly unintentionally present, particularly in MOCVD. Even though these act as shallow donors in β-Ga_2O_3, they become deep centers in $(Al_xGa_{1-x})_2O_3$ alloys. Based on interpolation of the $(+/-)$ transition levels, we find that $C_{(I)}$ acts as a compensating acceptor already at 5% Al, and H_i already at 1% Al.

Additionally, complex formation between hydrogen and either Si or C may occur. We found that Si_{cation}-H complexes have relatively low binding energy; if they form, they can probably quite easily be removed by annealing. C_{Ga}-H complexes are very stable and electrically neutral in *n*-type Ga_2O_3, and may explain why unintentionally incorporated carbon does not affect the carrier concentration [32]. C_{cation}-H complexes do act as acceptors in $(Al_xGa_{1-x})_2O_3$ alloys, but only if the Al concentration exceeds 56%. C_O-H, finally, was found to act as an acceptor over the entire range of alloy compositions, behaving very similarly to a N_O substitutional impurity and explaining experimental observations of carbon-related compensation in Ga_2O_3 grown by MOCVD [33,34].

Our findings indicate that the presence of hydrogen or carbon may interfere with controlled low-level Si doping in $(Al_xGa_{1-x})_2O_3$ alloys, and our detailed results can be used to devise growth or processing conditions to avoid this.

[1] H. Tippins, Phys. Rev. **140**, A316 (1965).

[2] T. Matsumoto, M. Aoki, A. Kinoshita, and T. Aono, Jpn. J. Appl. Phys **13**, 1578 (1974).

[3] C. Sturm, R. Schmidt-Grund, C. Kranert, J. Furthmüller, F. Bechstedt, and M. Grundmann, Phys. Rev. B **94**, 035148 (2016).

[4] A. Mock, R. Korlacki, C. Briley, V. Darakchieva, B. Monemar, Y. Kumagai, K. Goto, M. Higashiwaki, and M. Schubert, Phys. Rev. B **96**, 245205 (2017).

[5] M. Higashiwaki, K. Sasaki, A. Kuramata, T. Masui, and S. Yamakoshi, Appl. Phys. Lett. **100**, 013504 (2012).

[6] R. Suzuki, S. Nakagomi, Y. Kokubun, N. Arai, and S. Ohira, Appl. Phys. Lett. **94**, 222102 (2009).

[7] T. Oshima, T. Okuno, N. Arai, N. Suzuki, S. Ohira, and S. Fujita, Appl. Phys. Express **1**, 011202 (2008).

[8] F. Alema, B. Hertog, P. Mukhopadhyay, Y. Zhang, A. Mauze, A. Osinsky, W. V. Schoenfeld, J. S. Speck, and T. Vogt, APL Mater. **7**, 022527 (2019).

[9] Z. Feng, A. F. M. Anhar Uddin Bhuiyan, M. R. Karim, and H. Zhao, Appl. Phys. Lett. **114**, 250601 (2019).

[10] Y. Zhang, F. Alema, A. Mauze, O. S. Koksaldi, R. Miller, A. Osinsky, and J. S. Speck, APL Mater. **7**, 22506 (2019).

[11] N. Son, K. Goto, K. Nomura, Q. Thieu, R. Togashi, H. Murakami, Y. Kumagai, A. Kuramata, M. Higashiwaki, A. Koukitu, S. Yamakoshi, B. Monemar, and E. Janzen, J. Appl. Phys. **120**, 235703 (2016).

[12] A. Parisini and R. Fornari, Semicond. Sci. Technol. **31**, 035023 (2016).

[13] N. Ma, N. Tanen, A. Verma, Z. Guo, T. Luo, H. Xing, and D. Jena, Appl. Phys. Lett. **109**, 212101 (2016).

[14] M. Higashiwaki, A. Kuramata, H. Murakami, and Y. Kumagai, J. Phys. D **50**, 333002 (2017).

[15] N. Moser, J. McCandless, A. Crespo, K. Leedy, A. Green, A. Neal, S. Mou, E. Ahmadi, J. Speck, K. Chabak, N. Peixoto, and G. Jesse, IEEE Electron Device Lett. **38**, 775 (2017).

[16] A. T. Neal, S. Mou, S. Rafique, H. Zhao, E. Ahmadi, J. S. Speck, K. T. Stevens, J. D. Blevins, D. B. Thomson, N. Moser, and Others, Appl. Phys. Lett. **113**, 62101 (2018).

[17] M. Orita, H. Ohta, M. Hirano, and H. Hosono, Appl. Phys. Lett. **77**, 4166 (2000).

[18] T. Oishi, K. Harada, Y. Koga, and M. Kasu, Jpn. J. Appl. Phys. **55**, 30305 (2016).

[19] M. Higashiwaki, K. Sasaki, T. Kamimura, M. Hoi Wong, D. Krishnamurthy, A. Kuramata, T. Masui, and S. Yamakoshi, Appl. Phys. Lett. **103**, 123511 (2013).

[20] J. B. Varley, J. R. Weber, A. Janotti, and C. G. Van de Walle, Appl. Phys. Lett. **97**, 142106 (2010).

[21] J. B. Varley, A. Perron, V. Lordi, D. Wickramaratne, and J. L. Lyons, Appl. Phys. Lett. **116**, 172104 (2020).

[22] J. L. Lyons, D. Steiauf, A. Janotti, and C. G. Van de Walle, Phys. Rev. Applied **2**, 064005 (2014).

[23] J. B. Varley, H. Peelaers, A. Janotti, and C. G. Van de Walle, J. Phys.: Conden. Matter **23**, 334212 (2011).

[24] M. E. Ingebrigtsen, A. Y. Kuznetsov, B. G. Svensson, G. Alfieri, A. Mihaila, U. Badstübner, A. Perron, L. Vines, and J. B. Varley, APL Mater. **7**, 022510 (2019).

[25] H. von Bardeleben and J. Cantin, J. Appl. Phys. **128**, 125702 (2020).

[26] D. J. Chadi and K.-J. Chang, Phys. Rev. Lett. **61**, 873 (1988).

[27] L. Gordon, J. L. Lyons, A. Janotti, and C. G. Van de Walle, Phys. Rev. B **89**, 085204 (2014).

[28] H. Peelaers, J. B. Varley, J. S. Speck, and C. G. Van de Walle, Appl. Phys. Lett. **112**, 242101 (2018); **115**, 159901 (2019) (erratum).

[29] J. B. Varley, J. Mater. Res. **36**, 4790 (2021).

[30] Y. Zhang, C. Joishi, Z. Xia, M. Brenner, S. Lodha, and S. Rajan, Appl. Phys. Lett. **112**, 233503 (2018).

[31] H. P. Zhao (private communication).

[32] F. Alema, Y. Zhang, A. Osinsky, N. Orishchin, N. Valente, A. Mauze, and J. S. Speck, APL Mater. **8**, 021110 (2020).

[33] G. Seryogin, F. Alema, N. Valente, H. Fu, E. Steinbrunner, A. T. Neal, S. Mou, A. Fine, and A. Osinsky, Appl. Phys. Lett. **117**, 262101 (2020).

[34] F. Alema, Y. Zhang, A. Mauze, T. Itoh, J. S. Speck, B. Hertog, and A. Osinsky, AIP Adv. **10**, 085002 (2020).

[35] P. E. Blöchl, Phys. Rev. B **50**, 17953 (1994).

[36] G. Kresse and J. Hafner, Phys. Rev. B **48**, 13115 (1993).

[37] G. Kresse and J. Furthmüller, Phys. Rev. B **54**, 11169 (1996).

[38] K. Momma and F. Izumi, J. Appl. Crystallogr. **44**, 1272 (2011).

[39] J. Heyd, G. E. Scuseria, and M. Ernzerhof, J. Chem. Phys. **118**, 8207 (2003); J. Heyd and G. E. Scuseria, *ibid.* **124**, 219906 (2006).

[40] R. Franchy, G. Schmitz, P. Gassmann, and F. Bartolucci, Appl. Phys. A **65**, 551 (1997).

[41] C. Kranert, M. Jenderka, J. Lenzner, M. Lorenz, H. Von Wenckstern, R. Schmidt-Grund, and M. Grundmann, J. Appl. Phys. **117**, 125703 (2015).

[42] D. R. Lide, *CRC Handbook of Chemistry and Physics* (CRC Press, Boca Raton, FL, 2004), Vol. 85.

[43] R.-S. Zhou and R. L. Snyder, Acta Crystallogr. B **47**, 617 (1991).

[44] J. P. Perdew, K. Burke, and M. Ernzerhof, Phys. Rev. Lett. **77**, 3865 (1996).

[45] G. Henkelman, B. P. Uberuaga, and H. Jónsson, J. Chem. Phys. **113**, 9901 (2000).

[46] G. H. Vineyard, J. Phys. Chem. Solids **3**, 121 (1957).

[47] P. Weiser, M. Stavola, W. B. Fowler, Y. Qin, and S. Pearton, Appl. Phys. Lett. **112**, 232104 (2018).

[48] A. Janotti and C. G. Van de Walle, Phys. Rev. B **76**, 165202 (2007).

[49] C. Freysoldt, J. Neugebauer, and C. G. Van de Walle, Phys. Rev. Lett. **102**, 016402 (2009).

[50] C. Freysoldt, J. Neugebauer, and C. G. Van de Walle, Phys. Status Solidi B **248**, 1067 (2011).

[51] J. L. Lyons, A. Janotti, and C. G. Van de Walle, Phys. Rev. B **89**, 035204 (2014).

[52] J. L. Lyons and C. G. Van de Walle, npj Comput. Mater. **3**, 1 (2017).

[53] M. D. McCluskey, N. M. Johnson, C. G. Van de Walle, D. Bour, M. Kneissl, and W. Walukiewicz, Phys. Rev. Lett. **80**, 4008 (1998).

[54] C. Skierbiszewski, T. Suski, M. Leszczynski, M. Shin, M. Skowronski, M. Bremser, and R. Davis, Appl. Phys. lett. **74**, 3833 (1999).

[55] A. Bouzid and A. Pasquarello, Phys. Status Solidi RRL **13**, 1800633 (2019).

[56] M. Choi, J. L. Lyons, A. Janotti, and C. G. Van de Walle, Appl. Phys. Lett. **102**, 142902 (2013).

[57] C. G. Van de Walle and J. Neugebauer, Nature (London) **423**, 626 (2003).

[58] S. Mu, H. Peelaers, Y. Zhang, M. Wang, and C. G. Van de Walle, Appl. Phys. Lett. **117**, 252104 (2020).

[59] C. G. Van de Walle and J. Neugebauer, J. Appl. Phys. **95**, 3851 (2004).

[60] A. Venzie, A. Portoff, C. Fares, M. Stavola, W. B. Fowler, F. Ren, and S. J. Pearton, Appl. Phys. Lett. **119**, 062109 (2021).

[61] C. G. Van de Walle and J. Neugebauer, Annu. Rev. Mater. Res. **36**, 179 (2006).

[62] See Supplemental Material at http://link.aps.org/supplemental/10.1103/PhysRevB.105.155201 for the formation energy of Si_O and Si_O-H complexes in Ga_2O_3 and Al_2O_3.

[63] M. Choi, A. Janotti, and C. G. Van de Walle, ACS Appl. Mater. Interfaces **6**, 4149 (2014).

[64] H. Peelaers, J. L. Lyons, J. B. Varley, and C. G. Van de Walle, APL Mater. **7**, 022519 (2019).

[65] S. Lany, APL Mater. **6**, 046103 (2018).